Total cross sections of electron and positron collisions with C_3F_8 and C_3H_8 molecules and differential elastic and vibrational excitation cross sections by electron impact on these molecules

Hiroshi Tanaka, Yoshio Tachibana, and Masashi Kitajima
Department of Physics, Sophia University, Tokyo 102, Japan

Osamu Sueoka, Hideki Takaki, and Akira Hamada
Faculty of Engineering, Yamaguchi University, Ube, Yamaguchi 755, Japan

Mineo Kimura
School of Medical Sciences, Yamaguchi University, Ube, Yamaguchi 755, Japan
and Institute of Space and Astronautical Science, Sagamihara, Kanagawa 229, Japan
(Received 1 June 1998)

Total cross sections for electron (e^-) and positron (e^+) scattering from C_3H_8 and C_3F_8 have been measured from 0.8 to 600 eV and 0.7 to 600 eV, respectively. We have also investigated differential elastic cross sections by electron impact from 2.0 to 200 eV, and compared them with the present theoretical results. For e^- scattering from C_3H_8, the cross sections are found to be larger by a factor of 2 than those of e^+ scattering below 20–30 eV. They show a large peak at 8 eV due to a shape resonance and a shoulderlike structure in the region of 20–40 eV. For e^- scattering from C_3F_8, the cross sections are again larger by at least a factor of 2 than those of e^+ scattering below 50 eV, and they have two peaks at 4 and 8 eV, followed by a broad peak in the region of 20–40 eV. Some small structures overlie the broad hump. Both e^- and e^+ impact cross sections for C_3H_8 and C_3F_8 quickly approach each other beyond 200 eV. From the differential cross section study, we have been able to provide more detailed information on shape resonances, and also we have carried out some analysis of resonances in vibrational excitation results. In general, the total and integrated elastic cross sections are in good qualitative and quantitative agreement. [S1050-2947(99)04403-0]

PACS number(s): 34.80.Bm, 34.80.Gs

I. INTRODUCTION

Because of the basic importance for applications in plasma processing, a study of the total elastic and inelastic processes for electron scattering from various hydrocarbons including propane (C_3H_8) has attracted much experimental and theoretical attention and some explanatory studies about electron impact cross sections for small molecules have been reported (see Ref. [1] for further references). On the other hand, although it has become increasingly important as a reactive plasma etching gas, very few studies on fluorine-replaced hydrocarbons have been performed, and studies of propane, in particular octafluoropropane (C_3F_8), are practically nonexistent, and a set of electron impact cross sections for such processes relevant to production rates of a variety of radicals is urgently needed for applications [2]. It is known that a comparative study using positron impact on these gases is very effective for providing understanding of collision dynamics and interaction schemes, as we exemplified for CHF_3 [3]. For basic physics and chemistry, needless to say, both molecules are essential for an understanding of electronic structures and collision dynamics and interactions. The knowledge from the present study should be useful as a guiding principle for other hydrocarbon systems. A study of these large hydrocarbons, for which at present no systematic study exists, could provide new information on molecular physics. However, as very little comparative study exists for electron and positron impact, hence, almost no comprehensive collision data are available, which urges us to establish all cross-section data for applications.

We have conducted a joint experimental and theoretical study to give total and elastic scattering cross sections, to elucidate the similarity and difference of shape resonances between the two molecules, and to study angular distributions of the scattered electron.

We summarize some of the characteristic molecular constants for C_3H_8 and C_3F_8 in Table I for later discussions [4].

II. EXPERIMENTAL AND THEORETICAL SETUPS

A. Total cross-section (TCS) measurement

The experimental apparatus and the method have been reported earlier [5,6]. Briefly, a ^{22}Na radioisotope with an activity of 80 μCi and baked tungsten ribbons were used as the positron source and the positron moderator for low-

TABLE I. Molecular constants for C_3H_8 and C_3F_8. Data are from Ref. [4]. Note that X represents an H or F atom.

	C_3H_8	C_3F_8
C-X distance	1.102 Å	1.330 Å
C-C distance	1.512 Å	1.546 Å
C-C-C angle	112°	115.9°
X-C-X angle	108°	107°, 109°
Dipole moment	0.084 D	0.097 D

 ©1999 The American Physical Society

energy particles, respectively. For the electron source, slow electron beams (with an energy width of ≈1 eV) were produced after secondary electrons emitted from the same isotope were moderated by multiple scattering in the tungsten ribbons. The apparatus for the TCS measurement used for electron and positron impacts was a straight type time-of-flight (TOF) system, and a schematic diagram of the experimental arrangement has been shown earlier [5,6]. A retarding potential unit was combined with the TOF system for discrimination of elastically and inelastically scattered projectiles. The purity of C_3H_8 and C_3F_8 gases was 99.0% and 99.9%, respectively.

TCS values, Q_l are given by

$$Q_l = -(1/nl)\ln(I_g/I_v), \tag{1}$$

where n and l are the gas density in the collision cell and the effective length of the cell, respectively, and I_g and I_v are the beam intensity in the gas and vacuum, respectively. The effective length of the cell was derived by normalizing TCS's to those in the positron-N_2 data by Hoffman *et al.* [7]. The pressure independence of the TCS was confirmed by electron scattering at 8.5 and 9.0 eV for C_3H_8 and at 50 eV for C_3F_8.

The forward scattering due to the magnetic field and a large collision-cell aperture in the experiment should be distinguished from that of the unscattered beam. The correction for this effect should be included in the data analysis as previously described [8] where a simulation of each projectile under the conditions of geometry, external field, and scattering conditions was carried out to estimate the correction by examining if the projectile came through the scattering chamber. The same procedure for estimation of the correction was followed in the present study. The differential cross-section data for this correction both for electron and positron scattering were obtained from the combination of the present theoretical and elastic differential cross-section results. The correction for electron scattering amounts to 6–10 % below 70 eV, but it becomes much smaller at higher energies, amounting to less than 5% above 200 eV. For positron scattering, the corrections are generally found to be slightly larger than those for electron scattering. To assess the experimental errors, the relative error is estimated by summing all contributions from the intensity, $\Delta I/I$ (less than 1% for electron and 2–4 % for positron), where I represents $\ln(I_g/I_v)$, the gas density $\Delta n/n$ (=0.3%), and the effective length of the cell $\Delta l/l$ (=2%). Therefore, we assume that the experimental errors associated with total cross-section measurements would be less than 10% for both projectiles with slightly smaller errors for the electron case. The error arising from subtraction of the accidental coincidences in each channel is also included in the statistical errors.

B. Differential elastic cross-section (DCS) measurements

The experimental arrangement and procedures used in the present DCS measurements were similar to those in previous studies [9]. Briefly, the electron beam emerging from the monochromator is crossed at 90° with a molecular beam. The analyzer then measures the scattered electrons. In both the monochromator and the analyzer, a single hemispherical condenser is used for energy selection, and the imaging at variable energy is controlled by zoom lenses. The lens properties are carefully calculated by an electron trajectories program. To keep the transmission of the electrons constant, the programmable power supplies control the driving voltages of some lenses. Both the monochromator and the analyzer are enclosed in the differentially pumped boxes, respectively, to reduce the effect of the background gases and to minimize the stray electron background. The molecular beam was produced by effusing C_3H_8 through a simple nozzle with an internal diameter of 0.3 mm and a length of 5 mm. The spectrometer and the nozzle were heated to a temperature of about 50 °C to reduce contamination. The analyzer can rotate mechanically around the scattering center covering the angular range from −10° to 130° with respect to the incident electron beam. Due to an angular divergence of the incident electron beam and an acceptance angle of the analyzer, however, we cannot discriminate between the parent incident electrons and the scattered electrons for elastic scattering at the forward scattering angles below 15°–20°, especially in low impact energy regions.

During the present measurements, overall energy and angular resolutions are 30–40 meV [Full width at half maximum (FWHM)] and about ±1.5° respectively. Thus, the energy resolution is not sufficient to resolve the rotational excitations and adjacent vibrational bands as well. The incident electron energy is calibrated with respect to the 19.35 eV resonance of He and, for vibrational excitations, to the $^2\Pi_g$ resonances of N_2. The scattering spectrometers are operated in two ways. For the measurements of the elastic DCS, the intensity of the scattered electron signal is counted as a function of energy loss (the zero energy loss corresponds to the elastic scattering) at a fixed impact energy and scattering angle. To study resonances in vibrational excitations, the analyzer is set to transmit only signals corresponding to a specific energy-loss channel as a function of impact energy. Cross sections were obtained by the relative flow method [10] using helium as the comparison gas. The density distributions [11] for the two gases are assumed to be essentially identical by adjusting the pressure behind the nozzle with an approximate ratio of $P_{\mathrm{He}}:P_{\mathrm{C_3H_8}}=7:0.7$ (Torr). Experimental errors are estimated to be 15–30 % for elastic differential cross sections and 10–15 % for vibrational excitation cross sections.

For elastic scattering DCS's, the statistical errors are less than 3% where the accumulated counts are over 1500 counts for each scattering angle and incident energy in the present measurements. The errors associated with background contributions to the scattered signal are estimated to be less than 5% by using a side leak of the gas in place of the target gas line. The incident electron current was found to be constant within 3% over the duration of the present experiment. The relative pressure readings of the capacitance manometer are claimed to be accurate to better than 1%. In the relative flow technique employed here, we estimate the error for the measurements of the ratio, DCS(C_3H_8 and C_3F_8)/DCS(He), as about 11%, which is the square root of the sum of the squares for these errors. The value of the DCS's (C_3H_8 and C_3F_8) was then obtained by multiplying the ratio to the standard value of the He DCS. The estimated error in the DCS (He) is determined to be 10%. Therefore, the estimated error in the present DCS measurement is about 15% at most. For the vibrational excitation DCS, the estimated error of about

30% is due mainly to the combined errors associated with the numbers of the accumulated counts of 10% (minimum of 100 counts), the empirical background subtraction in a long tail on the high-energy side of 20%, and the elastic DCS of 15%. The errors in the integral, Q_I, and momentum transfer cross sections, Q_M, are estimated to be about 30%, which comes from the 15% uncertainty in the elastic DCS and about an additional 20% error due to the extrapolation. Note that the momentum transfer integrations have relatively larger errors since the Q_M integration depends more heavily on the large-angle elastic DCS extrapolation. Details of this method are presented in Refs. [10] and [11].

C. Theoretical model

The theoretical approach employed is the continuum multiple-scattering (CMS) method, which is a simple but efficient model for treating electron scattering from polyatomic molecules [12]. In short, to overcome difficulties arising from (i) the many degrees of freedom of electronic and nuclear motions and (ii) the nonspherical molecular field in polyatomic molecules, the CMS divides the configuration space into three regions: region I, the atomic region surrounding each atomic sphere (spherical potentials); region II, the interstitial region (a constant potential); and region III, the outer region surrounding the molecule (a spherical potential). The scattering part of the method is based on the static-exchange-polarization potential model within the fixed-nuclei approximation. The static interaction is constructed by the electron density obtained from the CMS wave function, and the Hara-type free-electron gas model [12] is employed for the local-exchange interaction, while the polarization interaction is considered for only terms proportional to r^{-4}. A simple local-exchange potential replaces the cumbersome nonlocal-exchange potential making the practical calculation tractable.

Under these assumptions, the Schrödinger equation in each region is solved numerically under separate boundary conditions. By matching the wave functions and their derivatives from each region, we can determine the total wave functions of the scattered electron and, hence, the scattering S matrix. Once the S matrix is known, the scattering cross section can be easily calculated. This approach has been tested extensively and is known to provide useful information on the underlying scattering physics [12]. Further, the CMS method is useful for interpolation and extrapolation for guiding experimental data points.

III. RESULTS

A. Total cross section (TCS) for electron and positron impacts on C_3H_8 and C_3F_8

Figures 1(a) and 1(b) present TCS's for both electron and positron impacts on C_3H_8 and C_3F_8 from 0.7 to 600 eV, respectively. First we discuss the results from electron scattering, followed by the results from positron scattering.

1. Electron scattering

New aspects found can be summarized as follows.

(i) Both C_3H_8 and C_3F_8 cross sections have a peak around 8–9 eV and that for C_3F_8 has a second peak near 25 eV. The first peak observed at 8–9 eV is common to both molecules and is due to a shape resonance arising from the temporary trapping of the electron in antibonding C-H (F) orbitals, and the second peak in C_3F_8 at 25 eV is also due to a combination of shape resonances from a few of the higher unoccupied orbitals in this energy region. It appears that for C_3F_8, there is a weak peak around 4 eV.

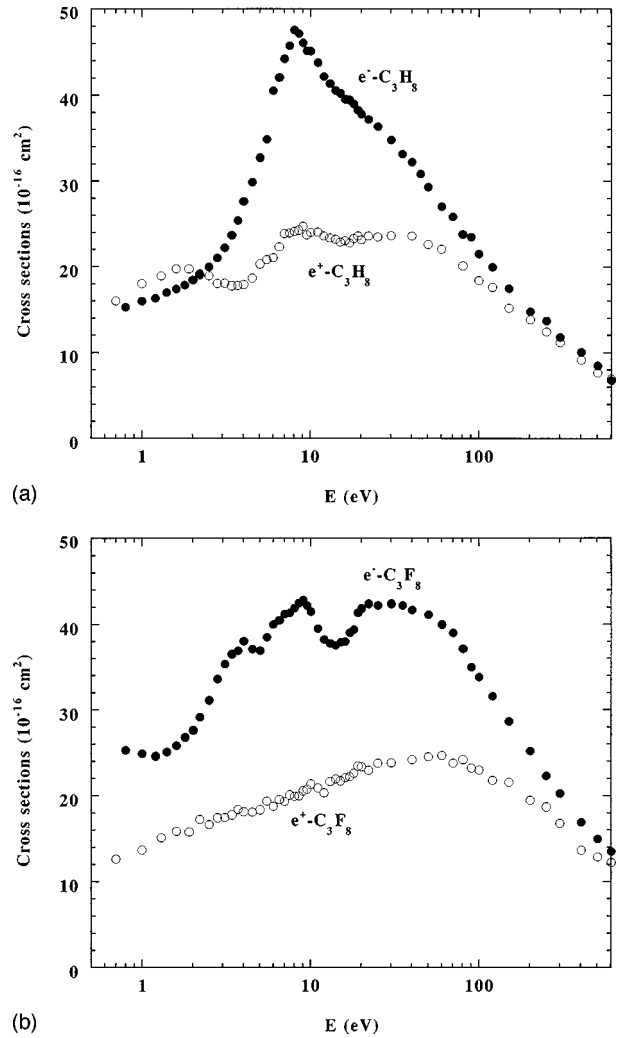

FIG. 1. Total cross sections for (a) C_3H_8 and for (b) C_3F_8 both by electron (●) and positron (○) impact.

(ii) Both cross sections decrease rather sharply below 7–8 eV for C_3H_8 and below 4 eV for C_3F_8. Since these are polar molecules (with the values of the dipole moments being 0.084 and 0.097 D for C_3H_8 and C_3F_8, respectively), their cross sections should come back again at much lower energies, and turn to the increasing trend. It has been shown [2] that the total electron scattering cross section is below thermal energies for strongly polar molecules as $\sigma_{\mathrm{tot}} \sim (A/v^2)$, where A is a constant and v is the speed of the electron (positron), respectively. This suggests that the cross section increases as the inverse of the collision energy near thermal energies.

(iii) Both cross sections also decrease beyond the first (third) peak for C_3H_8 (C_3F_8) gradually above 25–30 eV.

(iv) Except for the region of 6–18 eV, the cross section for C_3F_8 is consistently larger, and at both ends of the energy studied, the difference between the two TCS's is nearly a

factor of 2. This difference in magnitude should be the reflection of the difference in molecular sizes related to H and F atoms attached, and can be interpreted by using a perturbative method such as the Born treatment at higher-energy regions.

2. Positron scattering

The results are also included in Figs. 1(a) and 1(b). Specific features seen are summarized for this case.

(i) Two shapes of the cross sections are rather different below 50 eV, that is, for C_3H_8 the cross sections have three visible structures at around 2, 8, and 30 eV, while for C_3F_8 they are much smoother without any obvious structure except for a maximum at around 40 eV. It is interesting to note that the peak position at 8 eV in C_3H_8 by e^+ impact is nearly equivalent to that for e^- impact. The peak for the positron is due to the combination of positronium formation and electronic excitation and ionization, while that for the electron is, as stated, due to the shape resonance.

(ii) The maximum magnitude of the cross sections is rather similar, namely both appear to have a size approximately $2.2\times10^{-15}\,\mathrm{cm}^2$ at a peak around 20–30 eV. In addition, that for C_3H_8 drops somewhat faster at the higher-energy region than that for C_3F_8 and at 500 eV, for example, the cross section for C_3H_8 reaches $8\times10^{-16}\,\mathrm{cm}^2$ while that for C_3F_8 is approximately $12\times10^{-16}\,\mathrm{cm}^2$. This different behavior at higher energy is a consequence of the size of the molecule as well as the stronger interaction from F atoms in C_3F_8.

The definite cause of the three strong peaks seen in C_3H_8 is not obvious, but at least for the one at the lowest energy we suspect that the positronic propane may possibly be formed by being temporarily trapped in the outer tail of the molecular field. For C_3F_8, the F atom has a stronger electron negativity than a carbon atom, and hence the F atom charges negatively, while for C_3H_8, contrarily, the H atom is positively charged. Therefore, an incoming positron sees a positive charge when it approaches the C_3H_8 molecule, while for C_3F_8 it sees the negative charge. Because of a larger number of electrons in C_3F_8, the incoming positron is properly screened by the molecular electrons, causing weaker perturbation to the molecule and hence weaker structure. This resonance state is not stable, even if ever formed, against electron-positron annihilation, and decays through two γ-ray emissions, or the positron escapes through tunneling. Based on a simple general formula for the annihilation rate [13], we can estimate the approximate rate with a value on the order of $10^{10}\,\mathrm{sec}^{-1}$, which is about four times faster than that of the PsH complex owing to a larger amount of electrons in this molecule.

3. Comparison between electron and positron scattering

Some unique features emerge when comparing these two sets of the results, and they are summarized as follows.

(i) The magnitude of the total cross sections for C_3H_8 by e^+ impact is far smaller than that of e^- impact at almost all energies, and for intermediate energies the magnitude is less than half. But the situation reverses below a few eV for C_3H_8, causing the cross section of e^+ impact to become larger than that of e^- impact. This feature may be due to a larger cross section for some channels in rovibrational excitations by e^+ impact than that by e^- impact, as we have pointed out earlier [14].

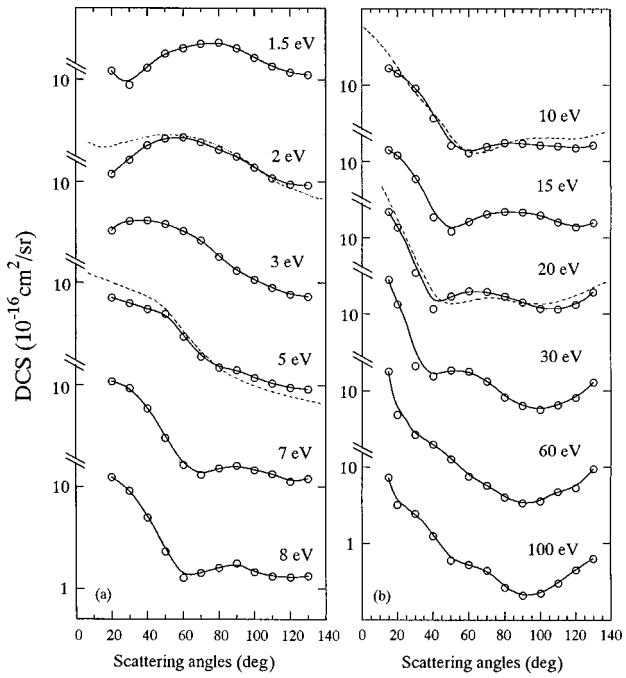

FIG. 2. Differential elastic cross sections for a C_3F_8 molecule by electron impact for (a) low scattering energies below 8 eV and (b) higher energies above 10 eV. The dashed line is the present theoretical elastic cross section for electron scattering based on the CMS method.

(ii) On the contrary, the magnitude of the total cross section C_3F_8 by e^+ impact is consistently smaller than that of e^- impact at all energies studied, and no reverse situation of the cross section is found. We speculate that the reason for this is that for C_3F_8, a rovibrational energy spacing is larger than that for C_3H_8 in combination of the stronger dipole moment, and hence the reverse order of the cross section may be possible at much lower energy nearer to the threshold, which is beyond the present experimental energy range.

(iii) For the resonance peak around 10 eV for C_3H_8 and C_3F_8 by e^- impact, the peak seen in C_3H_8 is larger in magnitude than that for C_3F_8. This may be due to a smaller contribution from vibrational excitation of C_3F_8 because of heavier F atoms.

(iv) Both e^+ and e^- impact cross sections appear to merge beyond 200 eV, the reason being apparent from the Born argument. However, the difference between C_3H_8 and C_3F_8 of two sets of the cross section by e^- and e^+ impacts is vastly different. The difference for C_3H_8 becomes much smaller at lower collision energies of 30–40 eV, while it begins to narrow only beyond 100 eV for C_3F_8. This disparity is an apparent reflection of the size of the charge distribution between H and F atoms. In other words, we can ''see'' the wave functions of C_3H_8 and C_3F_8 by comparing high-energy e^- and e^+ impacts.

B. Differential cross sections (DCS's) for C_3F_8

The DCS's for C_3F_8 with respect to the scattering angle measured are illustrated graphically in Figs. 2(a) and 2(b) for

TABLE II. Numerical data of elastic scattering DCS's for C_3H_8. Given at the bottom are integrated elastic cross sections Q_I and momentum-transfer cross sections Q_M calculated based on the procedure described in the text with Eqs. (2a) and (2b) (in units of 10^{-16} cm^2).

	Impact energy																
θ	1.5 eV	2 eV	3 eV	4 eV	5 eV	6.5 eV	7 eV	8 eV	9 eV	10 eV	12 eV	15 eV	20 eV	25 eV	30 eV	60 eV	100 eV
15										16.748	15.202	14.168	22.021	26.080	28.094	17.724	7.253
20	1.224	1.185	3.270	5.757	7.099	9.769	10.830	12.417	14.415	14.339	12.969	12.032	13.724	14.267	13.322	4.860	3.174
30	0.883	1.624	4.100	6.171	6.284	9.395	9.306	9.099	9.232	9.051	7.671	5.932	3.473	2.665	2.098	2.683	2.436
40	1.309	2.258	4.143	6.085	5.510	5.981	5.916	4.958	4.154	3.662	3.083	1.866	1.161	1.565	1.551	2.007	1.251
50	1.792	2.632	3.811	4.941	4.940	3.409	3.048	2.313	1.595	1.608	1.417	1.217	1.689	2.010	1.844	1.276	0.596
60	2.033	2.718	3.250	3.739	2.946	1.900	1.642	1.280	1.253	1.289	1.481	1.628	1.978	2.132	1.776	0.751	0.525
70	2.232	2.418	2.618	2.436	1.889	1.356	1.303	1.429	1.612	1.549	1.767	2.046	1.945	1.908	1.328	0.571	0.442
80	2.290	2.034	1.811	1.773	1.474	1.375	1.516	1.603	1.669	1.751	1.906	2.204	1.684	1.225	0.825	0.397	0.263
90	2.038	1.752	1.323	1.315	1.391	1.435	1.613	1.777	1.650	1.716	1.959	2.168	1.418	0.813	0.640	0.334	0.207
100	1.640	1.369	1.075	1.179	1.178	1.315	1.465	1.457	1.535	1.624	1.791	1.972	1.166	0.762	0.570	0.354	0.222
110	1.355	1.078	0.890	1.010	1.038	1.138	1.340	1.328	1.422	1.586	1.609	1.591	1.150	0.852	0.656	0.472	0.299
120	1.176	0.939	0.767	0.870	0.942	1.053	1.122	1.295	1.382	1.508	1.537	1.382	1.315	1.221	0.8127	0.530	0.449
130	1.115	0.916	0.734	0.872	0.908	1.081	1.199	1.334	1.580	1.623	1.590	1.569	1.929	1.645	1.283	0.942	0.632
Q_I	19.800	20.817	27.401	35.317	37.503	42.877	44.365	44.513	44.942	44.335	42.379	39.150	37.631	36.324	32.869	18.784	13.001
Q_M	18.244	17.524	21.909	26.542	32.918	35.031	33.888	38.513	41.088	40.784	38.193	35.610	31.745	26.921	23.625	16.713	10.376

several scattering angles, and the numerical data are included in Tables II and III. In Fig. 3, we have included some of representative results from both C_3H_8 and C_3F_8 for a comparative study in the same scattering energies and angles. A comparison between these molecules provides much information on collision dynamics and interactions. First we discuss the DCS's for C_3F_8 only, followed by a comparison between two molecules. Unfortunately no directly comparable experimental data are available in the literature.

1. Elastic DCS at 2–7 eV

The elastic DCS's at lower incident energies are shown in Fig. 2(a). The overall angular behavior for the weak polar molecule of C_3F_8 (0.097 D) is very similar to those of the same saturated fluorocarbon molecules of CF_4 [15] and C_2F_6 [16] (nonpolar perfluoroalkanes). At 2 eV, it shows a decreasing trend toward smaller angles around the 20°–50° region and a conspicuous, strong hump at intermediate angles around 60°. In the case of CF_4, however, this behavior is not reproduced by the calculations [17,18]. For the CF_4 molecule studied by *ab initio* methods, it is essential to include more basis functions on the fluorine atoms, and to include additional diffuse functions in order to obtain converged results of electronic energies. Unfortunately, the experimental angular range could not be extended to lower angles below 20° due to the parent electron beam contributions, as mentioned above. The hump is found to move toward smaller angles becoming a monotonous increase near the zero angle region. As the energy increases near 5 eV, it becomes just a small shoulder around 60° (as has been often observed in every linear-chain molecule), smoothly decreasing at much larger angles. As the energy slightly increases to 6–7 eV, a new structure emerges around 100°. This energy region corresponds to the position of a shape resonance through the trapping of the incident electron in an antibonding C-F (H) orbital (a temporary negative ion, for simplicity called TNI). This TNI is common to most saturated hydrocarbons [19], in which we have seen the signature of TNI both in the total and elastic integral cross sections. But, the structures or undulations in the DCS's change continuously as a function of the incident energies and the scattering angles. In the elastic scattering, because the DCS's result in the sum of partial waves of resonant and nonresonant contributions, a conspicuous resonant feature is normally somewhat washed out. However, the resonances are more clearly visible in the inelastic scattering, and hence a study of vibrational excitation is important and essential for a basic understanding of the dynamics (see Sec. III B 5).

2. Elastic DCS at 8–100 eV

The elastic DCS's for higher energies are presented in Fig. 2(b). For energies above 7 eV, as already mentioned, the DCS's show a steep increase toward the zero scattering angle. The new hump shown up at 7 eV begins to shift toward smaller angles as the scattering energy increases, and it becomes most conspicuous at 60° and at 30 eV. Again, it is indeed the energy region where a hump is seen in the total cross section as well as the elastic integral cross section. The

TABLE III. Vibrational term symbols belonging to A_1 symmetry only, and energy-loss positions for the single peaks of the spectral decompositions (major components only).

	$\nu1$	$\nu2$	$\nu3$	$\nu4$	$\nu6$	$2\nu1$	$2\nu2$	$2\nu4$	$3\nu1$	$3\nu2$	$\nu1+\nu3$	$\nu1+\nu7$	$2\nu1+\nu7$	$\nu3+\nu4$
Energy (eV)	0.1699	0.1610	0.1432	0.0967	0.0824	0.3398	0.3220	0.1934	0.5097	0.483	0.3131	0.2173	0.3872	0.2399

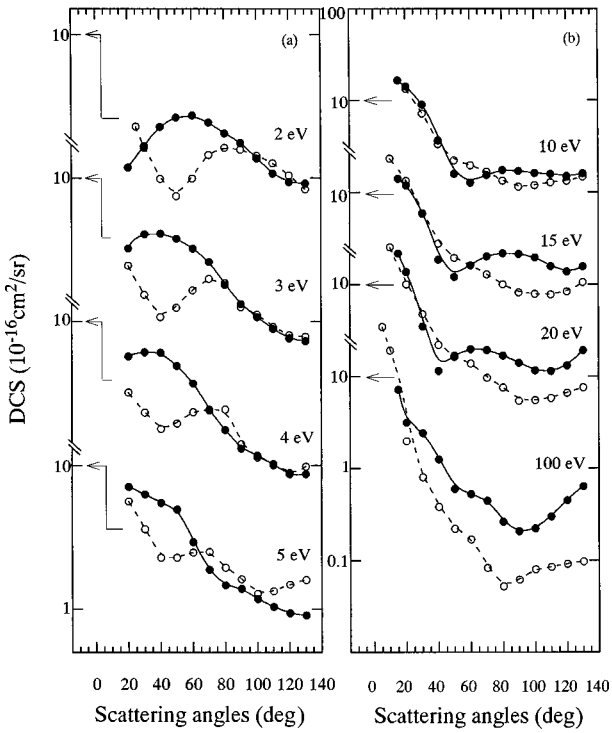

FIG. 3. Comparison of the DCS's for both C_3H_8 (○) and C_3F_8 (●) molecules (a) below 5 eV and (b) above 5 eV.

ionization threshold starts above 11 eV. At 100 eV, this resonance structure becomes far weaker, but as has been observed in other hydrocarbons and fluorocarbons, the DCS is undulated moderately for the forward scattering direction due to the interference of the scattering waves from the composite atoms. Included in the figure is the CMS result, and it follows this experimental result reasonably well. Particularly, it reproduces well a shallow minimum at 40°–50° in the 10–20 eV region.

3. Comparison of DCS's between C_3H_8 and C_3F_8

Some representative DCS's for these two molecules are illustrated at incident energies of 2–100 eV in Figs. 3(a) and 3(b).

(i) At 2 eV, the shape of the DCS for C_3H_8 shows a minimum at 40° and begins to increase below this angle, while that for C_3F_8 shows a maximum at 60° and keeps decreasing for smaller angles. In addition, the hump at 80° seen in C_3H_8 moves toward a much smaller angle of 55° for C_3F_8. Both humps are from the same origin, i.e., due to the shape resonances discussed later. Because of a large electron charge distribution for C_3F_8, the incident electron feels a stronger influence from F atoms resulting in larger structures even at much smaller angles (larger distance).

(ii) When the incident energy increases to 5 eV, the DCS for C_3H_8 has a clear hump at 80° while that for C_3F_8 has no obvious structure in the same angular region.

(iii) As the energy reaches 7 eV, contrary to the 5 eV case, the DCS for C_3F_8 has a weak structure at 90° while that for C_3H_8 wiggles slightly at 10 eV, but no strong structures are found. These shifts of position of structures correspond to the difference of orbital energies between C_3H_8 and C_3F_8 (much higher partial waves are expected to contribute to the scattering for C_3F_8 within the partial-wave approximation).

(iv) At much higher energies, the DCS's for C_3F_8 still show a clear structure at 60°–70° while those for C_3H_8 have already become the typical feature of the DCS, i.e., a steep increase at small angles and a sharp drop as the scattering energy increases.

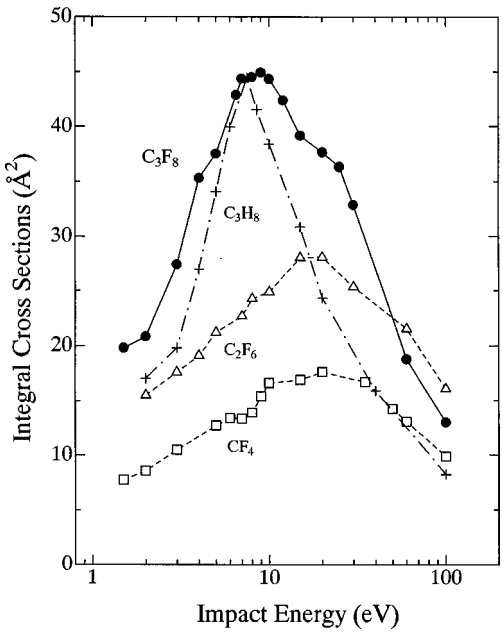

FIG. 4. Integrated elastic cross sections for C_3H_8, C_3F_8, C_2F_6, and CF_4 as designated in the figure.

4. Integral cross sections

Figure 4 shows integral cross sections and the numerical results of the data are included in Table II for C_3H_8, along with those of momentum transfer cross sections. The integral as well as momentum transfer cross sections were obtained from the following relations:

$$Q_I = 2\pi \int X_{\mathrm{DCS}}(\theta) \sin\theta \, d\theta \tag{2a}$$

and

$$Q_M = 2\pi \int X_{\mathrm{DCS}}(\theta)(1-\cos\theta) \sin\theta \, d\theta. \tag{2b}$$

To carry out these integrations, the DCS's of Figs. 2(a) and 2(b) have been extrapolated both to 0° and 180°, approximately based on a modified phase-shift analysis used for many different molecules in our laboratory [20]. As for the more direct, and perhaps more promising experimental approach, a dipole magnetic-field technique developed recently in the Manchester group [21] could be employed for the direct scattering measurements at the forward (near 0°) and backward (near 180°) angle regions, and we are now in preparation to install this capability in our facilities. The overall error arising from the present procedure is less than 30% since the extrapolation is known to affect the minor portion of the integration.

Both cross sections for C_3H_8 and C_3F_8 show a strong peak at 7.5 eV and around 9 eV, respectively, in which the mag-

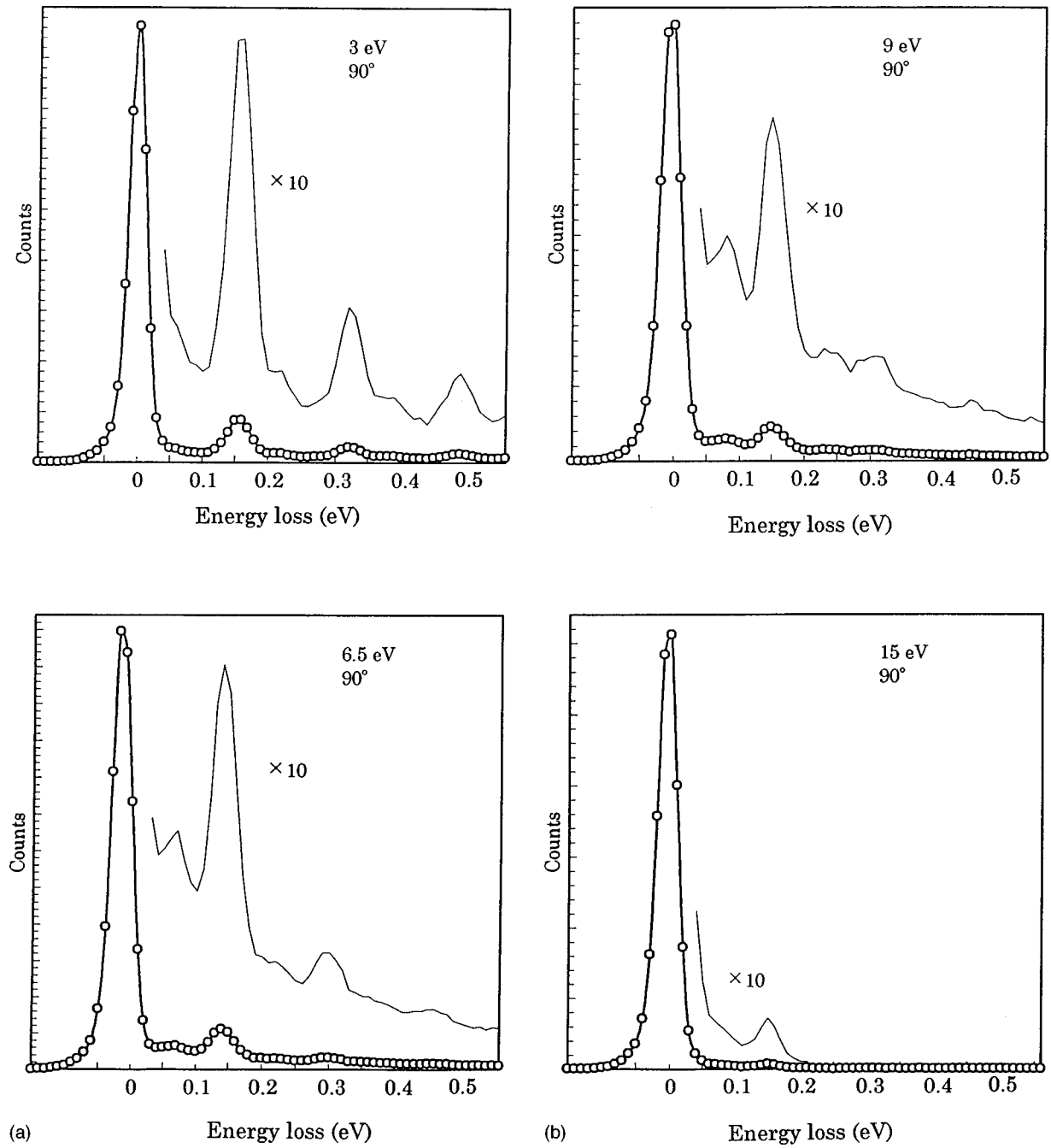

FIG. 5. Energy-loss spectra of C_3F_8 at a scattering angle 90°, for the incident energies of (a) 3 eV and 6.5 eV and (b) 9 eV and 15 eV.

nitude for C_3H_8 is nearly equivalent to that of C_3F_8, but the peak of C_3H_8 is much sharper and narrower. No other structure is observed for C_3H_8 within the present energy domain. The cross sections for C_3F_8 are larger in magnitude, and clearly reveal two other shoulders at 4 and 25 eV. As we discussed below (see Sec. III B 5), more specifically, these shoulders come from, we suspect, contributions of inelastic channels. Indeed, there is a great deal of evidence for strong vibrational excitation in these energy ranges. Moreover, these structural features are consistent with the situation of the total cross section shown in Fig. 1 as discussed below in Sec. III C.

Included in Fig. 4 are the integral elastic cross sections for our previous cross sections of CF_4 and C_2F_6 for a comparison. The reasons we compare with these molecules are twofold: (i) because of the prominent shape resonance at around 20 eV, characteristic of F-containing hydrocarbons, it is interesting to see how the resonance shows up in C_3F_8 (see Fig. 6), and (ii) CF_4 and C_2F_6 are known to show similar features in total cross sections in our earlier study, and hence it is important to see the systematics when one goes from C_2F_6 to C_3F_8. Apparently the peak positions for these two gases are different from the present C_3H_8 and C_3F_8 with the position being shifted to much higher energies at 18 and 20 eV for CF_4 and C_2F_6, respectively. Furthermore, both magnitudes at the peaks are much smaller than those of C_3H_8 and C_3F_8. This increasing trend of the peak magnitude as the number of atoms increases has been seen earlier for other systems such as CH_4, C_2H_6, and C_3H_8. Both cross sections

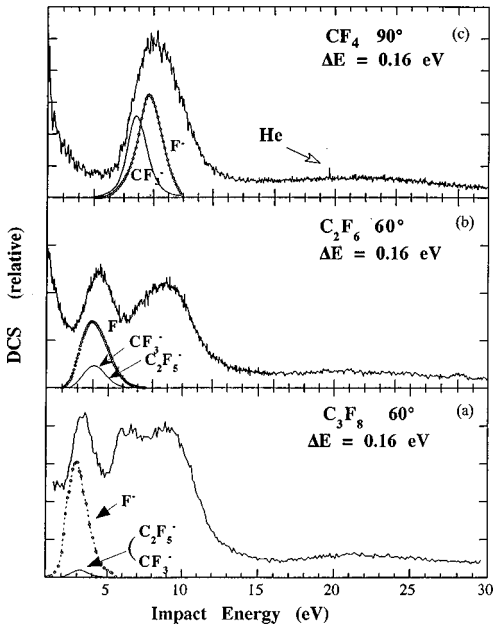

FIG. 6. Vibrational excitation functions of the energy-loss (0.16 eV) peaks due to the stretching mode for (a) C_3F_8 (60°), (b) C_2F_6 (60°), and (c) CF_4 (90°) together with dissociative attachment cross sections [26]. In (a) and (b), the small solid line corresponds to CF_3^- and $C_2F_5^-$, which are nearly identical in magnitude, and the dotted line with circles corresponds to F^- formation. In (c), the small solid line is for CF_3^- and the small spike corresponds to He resonance at 19.36 eV.

for CF_4 and C_2F_6 can be seen to decrease toward the Ramsauer-Townsend minimum below 0.5 eV.

5. Vibrational excitation

Composite energy-loss spectra of C_3F_8 are shown in Fig. 5 at 3, 6.5, 9, and 15 eV incident electron energies for a scattering angle of 90°. As mentioned earlier, the present energy resolution (30–40 meV) is not sufficient to resolve individual vibrational modes (including 25 fundamental modes [22] and their overtones) of the four prominent compound peaks at 0.09 eV (C-C stretching and C-F deformation vibrations), 0.16 eV (mainly C-F stretching vibrations), 0.32 eV, and 0.48 eV (their combinations and overtones). A strong enhancement is seen, however, in the resonance region where harmonics is enhanced, specifically, at 3 eV, and weak peaks are seen to appear at 6.5 and 9 eV in the 0.09-eV loss mode. But no such feature is found in the nonresonant energy at 15 eV. The corresponding excitation function for the 0.16 eV energy loss due to the stretching modes is also presented as a function of the impact energy for a scattering angle of 60° in Fig. 6, together with our previous results of CF_4 (90°) and C_2F_6. These DCS's are normalized to those of He by means of the relative-flow method. Again, enhancements appear distinctly at 3, 6.5, 9, and 21 eV, respectively, which provide sufficient evidence for the shape resonances. In these three perfluoroalkanes, as the number of atoms in a molecule increases, new narrower resonances begin to show up as the incident energies lower. But, a very weak and broad feature remains at the same energy of 21 eV, which was discussed for CF_4 by Huo [23]. Except for the hump in

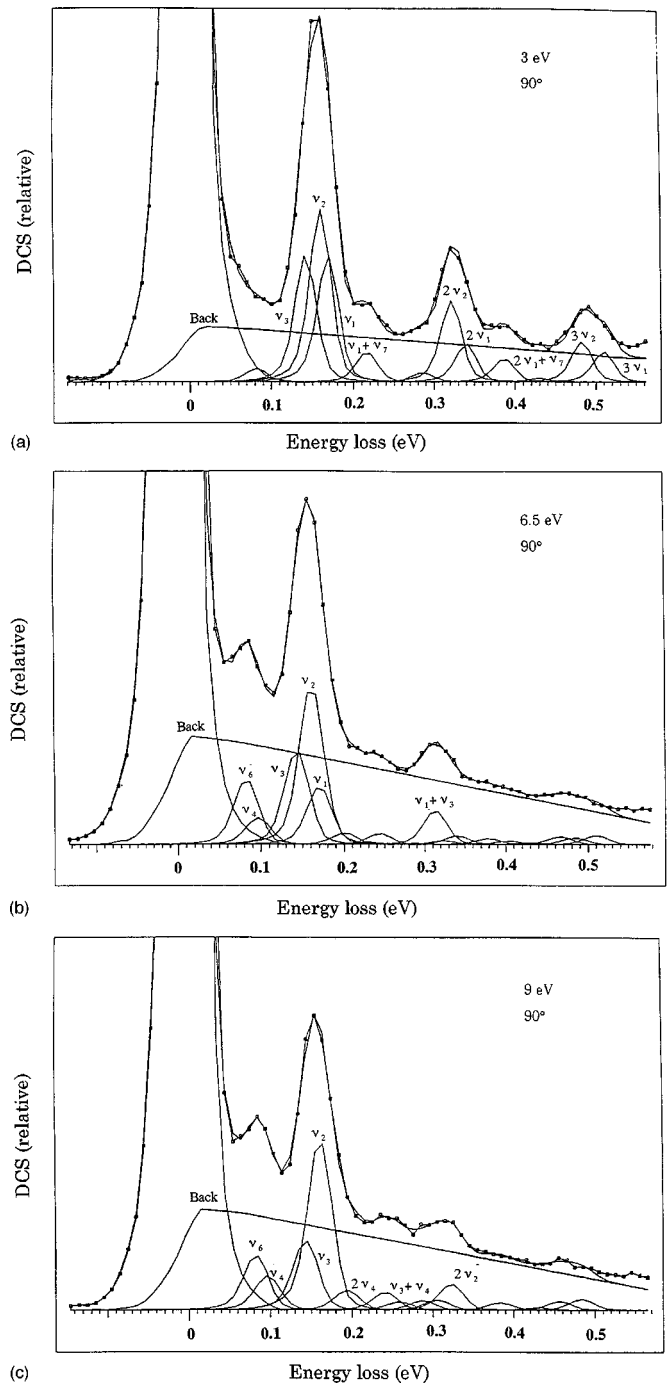

FIG. 7. Spectral decompositions of the energy-loss spectra of Fig. 5 into vibrational modes of species A_1 listed in Table II. The vibrational term symbols for major components only are shown.

C_3F_8 at 3 eV, the remaining three peaks coincide with the structures seen in the total cross section and the elastic integral cross section.

To investigate strong selectivity in vibrational excitation due to the shape resonances in some detail, vibrational modes tentatively decomposed are also included in Fig. 7, which belong only to the $A1$ irreducible representation. Considering the spectrum that is composed of a superposition of modes in Table II, the spectral decomposition similar to that described earlier in [20] was employed. Briefly, apparatus functions for the fitting are estimated from the elastic DCS peak of He by subtracting empirically a long tail on the

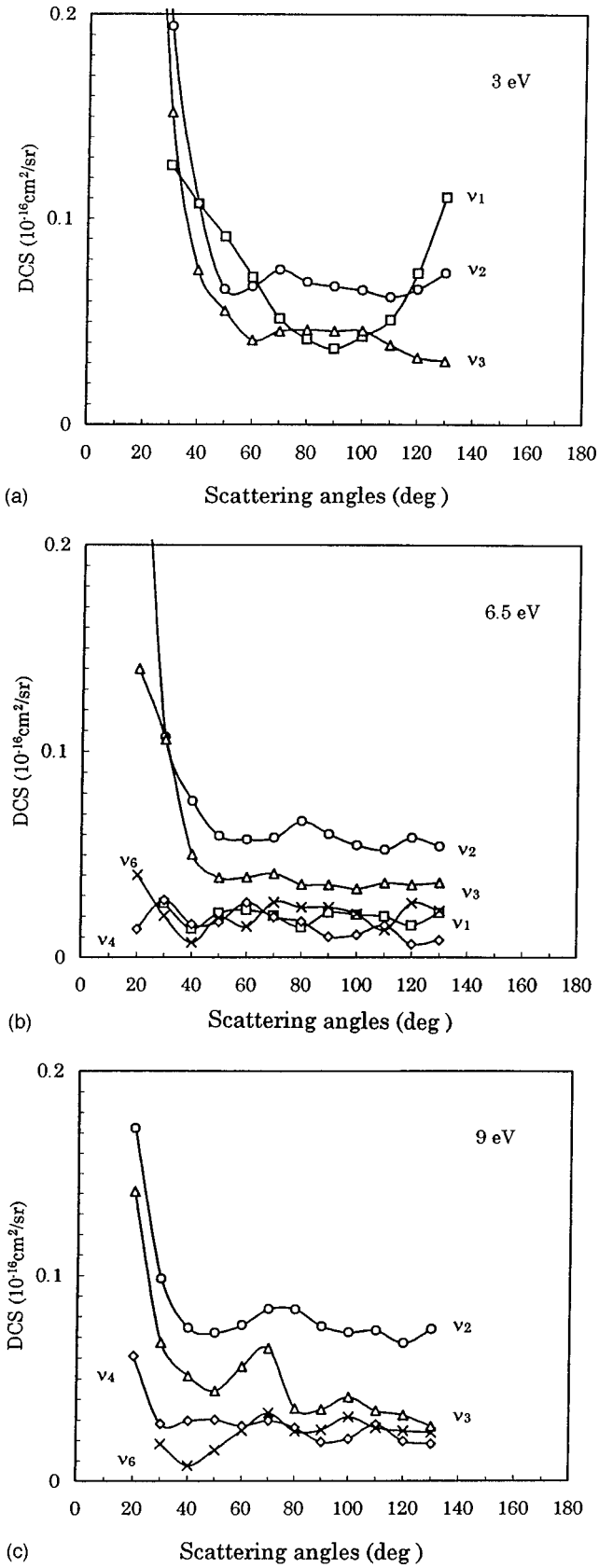

FIG. 8. The angular distributions in the decomposed v_1, v_2, and v_3 modes for (a) 3 eV, (b) 6.5 eV, and (c) 9 eV.

high-energy side due to the background noise. Then a least-squares-fitting procedure is employed to determine the intensity of the individual mode up to 0.55 eV as shown in Fig. 7. In general, the temporary negative ion (TNI) is produced through a temporal occupation of the lowest unoccupied molecular orbital (LUMO) by an incident electron. Based on the molecular structure calculation by using the GAUSSIAN-92 program [24], the LUMO is assumed to have the a_1 representation in the C_{2v} point group, and the mode into which it decays is given by the direct product $(A_1 \times A_1) = A_1$. Hence, the number of vibrational modes can be reduced to only $v_1 \sim v_9$ from the 25 fundamental modes. From this symmetry analysis, several important features emerge and should be noted. At 3 eV, v_1, v_2 (C-F_3 stretching), v_3 (C-F_2 stretching), and their overtone are enhanced strongly, but no evidence in the vibrational excitation of v_4 (C-C stretching) and v_6 (C-F_2 stretching deformation) is known to exist. But the v_4 and v_6 modes appear clearly at 6.5 and 9 eV, suggesting that these originate in different resonances from the one at 3 eV. On the contrary, the v_1 mode due to the C-C stretching becomes more prominent in the case of C_3F_8 at 4 and 9 eV. According to the angular correlation theory [25], the symmetry representation Γ_e of the scattered electron is again deduced from the direct product rule $(\Gamma_e \times a_1) = a_1$. Hence, the only electron-wave representation allowed is a_1 symmetry, and the scattered wave is contained in the first two angular momentum terms in $l=0$ and 1 in a target fixed-coordinate system. After transforming the fixed-coordinate frame to the laboratory frame [25], the angular distribution is characterized by a series of Legendre functions P_k with a maximum value of $k_{\max}=3$. The angular distributions of scattered electrons could, in general, give much detailed information on the resonances, but this simple theoretical procedure may not be appropriate to provide such an angular characteristic feature due to closely overlapping vibrational modes. Therefore, the angular distributions in the decomposed v_1, v_2, and v_3 modes are shown in Fig. 8 only as a reference. The simple theoretical treatment mentioned above, moreover, may be no longer applicable to such a case of two resonances with a close energy separation of 6.5 and 9 eV. Further information about the resonance may be obtained from a dissociative electron attachment measurement [26], in which only the TNI at 3 eV in C_3F_8 produces different types of an anion such as F^-, $C_2F_5^-$, and CF_3^-, as observed in CF_4 and C_2F_6 as well (see Fig. 6).

C. Comparison between total and elastic cross sections

We compare the total and integrated elastic cross sections as illustrated in Figs. 1 and 4 both for C_3H_8 and C_3F_8. As stated, the total cross section for C_3H_8 appears to be slightly larger than that of C_3F_8 at the peak region of 8–10 eV, which is consistent with the present trend of the integrated elastic cross section in Fig. 4. The present magnitude of the elastic cross section is smaller by 10–15% than the total at the peak. The inelastic scattering for rovibrational and, to a lesser extent, electronic excitations shows a pronounced dependence on the incident electron energy and thus accounts for the structural difference between the total and the elastic cross section as well. In practice, the weak structure around 15–40 eV for C_3F_8 matches that in the total cross section, which is much stronger due to contributions from electronic excitation (ionization) channels. Apparently, two measure-

ments for total and elastic processes are found to be consistent and in good qualitative as well as quantitative accord.

IV. CONCLUSIONS

We have investigated total scattering cross sections of C_3H_8 and C_3F_8 by e^- and e^+ impact in the incident energy region from 0.5 to 600 eV. Furthermore, we have investigated differential elastic cross sections of C_3H_8 and C_3F_8 in scattering angles from 20° to 130° at incident energies from 2 to 100 eV in conjunction with theoretical CMS calculation. The theoretical results follow reasonably well the experimental differential cross sections, and help identify the origin of some of the shape resonances observed. For e^- impact, strong shape resonances were found for both C_3H_8 and C_3F_8 molecules at 8 eV and at 4, 9, and 20–30 eV, respectively, which arise from the temporary trapping of the electron in antibonding orbitals. For e^+ impact, some wiggling structures in both cross sections were observed below 20 eV due probably to the resonance-type event (positronium formation in a molecule). The difference between the two sets of the cross sections by e^- impact and by e^+ impact for C_3H_8 is smaller at much lower incident energy, while that for C_3F_8 is much larger, around 300 eV, due to the larger size of this molecule. Because of the stronger electron negativity of F atoms in C_3F_8, the incident positron is effectively wrapped up by molecular electrons (positronium formation) resulting in a rather smooth cross section, while for C_3H_8, H atoms are positively charged, causing stronger interaction with the incoming positron and, hence, some conspicuous structures in the cross section. We have also studied DCS's for elastic scattering both for C_3H_8 and C_3F_8 by e^- impact below 100 eV. The hump is found in DCS's at lower energies, but as the energy increases near 5 eV, it becomes just a small shoulder around 60°. This hump is due to a shape resonance through the trapping of the incident electron in an antibonding C-F (H) orbital which is common to most saturated hydrocarbons. The resonances are more clearly visible in the inelastic scattering, and hence a study of vibrational excitation is carried out for detailed elucidation. We compare the total and integrated elastic cross sections both for C_3H_8 and C_3F_8. The total cross section for C_3H_8 appears to be slightly larger than that of C_3F_8 at the peak region of 8–10 eV, which is consistent with the present trend of the integrated elastic cross section. The present magnitude of the elastic cross section is found to be smaller by 10–15 % than the total at the peak. The inelastic scattering for rovibrational and, to a lesser extent, electronic excitations shows a pronounced dependence on the incident electron energy and thus accounts for the structural difference between the total and the elastic cross section as well.

ACKNOWLEDGMENT

The work has been supported in part by a Grant-in-Aid from the Ministry of Education, Science and Culture and the Institute of Space and Astronautical Sciences (M.K.).

[1] L. G. Christophorou, J. K. Olthoff, and M. V. V. S. Rao, J. Phys. Chem. Ref. Data **25**, 1341 (1996).
[2] L. G. Christophorou, J. K. Olthoff, and M. V. V. S. Rao, J. Phys. Chem. Ref. Data **26**, 1 (1997).
[3] O. Sueoka, H. Takaki, A. Hamada, H. Sato, and M. Kimura, Chem. Phys. Lett. **288**, 124 (1998).
[4] H. G. Mack, M. Dakkouri, and H. Oberhammer, J. Phys. Chem. **95**, 3136 (1991).
[5] O. Sueoka and S. Mori, J. Phys. B **19**, 4035 (1986).
[6] O. Sueoka, S. Mori, and A. Hamada, J. Phys. B **27**, 1453 (1994).
[7] K. R. Hoffman, M. S. Dababneh, Y.-F. Hsieh, W. E. Kauppila, V. Pol, J. H. Smart, and T. S. Stein, Phys. Rev. A **25**, 1393 (1982).
[8] A. Hamada and O. Sueoka, J. Phys. B **27**, 5055 (1994).
[9] H. Tanaka, L. Boesten, D. Matsunaga, and T. Kudo, J. Phys. B **21**, 1255 (1988).
[10] S. Srivastava, A. Chutjian, and S. Trajmar, J. Chem. Phys. **63**, 2659 (1975).
[11] R. T. Brinkman and S. Trajmar, J. Phys. E **14**, 24 (1979).
[12] M. Kimura and H. Sato, Comments At. Mol. Phys. **26**, 333 (1991).
[13] A. M. Frolov and V. H. Smith, Jr., Phys. Rev. A **55**, 2662 (1997).
[14] M. Kimura, O. Sueoka, A. Hamada, M. Takekawa, Y. Itikawa, H. Tanaka, and L. Boesten, J. Chem. Phys. **107**, 6616 (1997).
[15] L. Boesten, H. Tanaka, A. Kobayashi, M. A. Dillon, and M. Kimura, J. Phys. B **25**, 1607 (1992).
[16] T. Takagi, L. Boesten, H. Tanaka, and M. A. Dillon, J. Phys. B **27**, 5389 (1994).
[17] C. Winstead, Q. Sun, and V. Mckoy, J. Chem. Phys. **98**, 1105 (1993).
[18] K. L. Baluja, A. Jain, V. D. Marito, and F. A. Gianturco, Europhys. Lett. **17**, 139 (1992).
[19] H. Tanaka and L. Boesten, in *The 19th International Conference on Electron and Atom Collisions*, AIP Conf Proc. No. 360, edited by L. J. Dube, J. B. A. Mitchell, J. W. MacConkey, and C. E. Brian (AIP Press, New York, 1995), p. 279.
[20] M. A. Dillon, L. Boesten, H. Tanaka, M. Kimura, and H. Sato, J. Phys. B **26**, 3147 (1993).
[21] C. Cubric, T. Mercer, J. M. Channing, D. B. Thomson, D. R. Cooper, G. C. King, F. H. Read, and Zubek (unpublished).
[22] T. Shimanouchi, *Tables of Molecular Vibrational Frequencies*, Consolidated Vol. 1, NSRDS-NBS 39 (U.S. GPO, Washington, DC, 1972).
[23] W. M. Huo, Phys. Rev. A **38**, 3303 (1988).
[24] GAMESS is the package of the *ab initio* molecular structure calculation written by M. W. Schmidt *et al.*, J. Comp. Chem. **14**, 1347 (1993): M. J. Frisch *et al.*, 1992 GAUSSIAN 92 revision E1 (Gaussian Inc., Pittsburgh, PA, 1992).
[25] D. Andrick and F. H. Read, J. Phys. B **4**, 389 (1971).
[26] M. B. Spyrou, I. Sauers, and L. G. Christophorou, J. Chem. Phys. **81**, 4906 (1983).